nature catalysis

ARTICLES

https://doi.org/10.1038/s41929-018-0077-6

Boosting the performance of Cu_2O photocathodes for unassisted solar water splitting devices

Linfeng Pan[1,2], Jin Hyun Kim[3], Matthew T. Mayer[2], Min-Kyu Son[2,5], Amita Ummadisingu[2], Jae Sung Lee[3], Anders Hagfeldt[1], Jingshan Luo[2,4*] and Michael Grätzel[2*]

Although large research efforts have been devoted to photoelectrochemical (PEC) water splitting in the past several decades, the lack of efficient, stable and Earth-abundant photoelectrodes remains a bottleneck for practical application. Here, we report a photocathode with a coaxial nanowire structure implementing a Cu_2O/Ga_2O_3-buried p–n junction that achieves efficient light harvesting across the whole visible region to over 600 nm, reaching an external quantum yield for hydrogen generation close to 80%. With a photocurrent onset over +1 V against the reversible hydrogen electrode and a photocurrent density of ~10 mA cm^{-2} at 0 V versus the reversible hydrogen electrode, our electrode constitutes the best oxide photocathode for catalytic generation of hydrogen from sunlight known today. Conformal coating via atomic-layer deposition of a TiO_2 protection layer enables stable operation exceeding 100 h. Using NiMo as the hydrogen evolution catalyst, an all Earth-abundant Cu_2O photocathode was achieved with stable operation in a weak alkaline electrolyte. To show the practical impact of this photocathode, we constructed an all-oxide unassisted solar water splitting tandem device using state-of-the-art $BiVO_4$ as the photoanode, achieving ~3% solar-to-hydrogen conversion efficiency.

Hydrogen fuel generated through solar water splitting offers a green and sustainable energy source and addresses the issue of solar intermittency[1]. Although tremendous efforts have been devoted in the past several decades, there is still no solar water splitting device concurrently fulfilling the requirements of high efficiency, long-term stability and low cost[2,3]. The challenge remains that efficient photoelectrodes are generally composed of expensive semiconductor photoabsorbers and noble metal catalysts, while inexpensive and Earth-abundant photoelectrodes generally exhibit low efficiency. To overcome this dilemma, efforts are being focused in two main directions: searching for new materials and improving existing inexpensive photoelectrodes[3]. For the improvement of existing photoelectrodes, new benchmark performance is necessary to push the frontier of the field.

Due to their low cost, high abundance and facile preparation methods, metal oxide semiconductors play an important role in solar water splitting in both photocatalytic and photoelectrochemical (PEC) approaches[4,5]. Among them, Cu_2O is one of the most promising materials whose PEC performance in the water splitting reaction is the highest among all oxides. The modern era of Cu_2O photocathodes started with the seminal work by our group using atomic-layer-deposited protection layers to prevent Cu_2O from photodecomposition[6]. Subsequently, we improved the stability further by applying thicker TiO_2 protection layers and using RuO_x as the hydrogen evolution catalyst[7]. More recently, our group augmented the photocurrent density of the Cu_2O photocathode to 10 mA cm^{-2} at the reversible hydrogen electrode (RHE) potential using coaxial nanowire structures[8]. However, the photocurrent onset was at a voltage of only +0.5 V against the RHE. Inspired by Cu_2O photovoltaic cell developments[9–11], ref. [12] raised the onset of the photocurrent for a planar Cu_2O photocathode to 1.0 V for solar water splitting using Ga_2O_3 as an overlayer. However, the photocurrent rose only gradually to reach 2.9 mA cm^{-2} at the RHE potential, indicating that the planar architecture employed was ineffective in reconciling the light absorption depth required for efficient solar light harvesting with the much shorter minority carrier diffusion length of Cu_2O.

Here, we present a photocathode embodiment featuring a buried junction implemented in a coaxial nanowire structure that produces both a high photocurrent and photovoltage, fully addressing these challenges. The nanowire radial heterojunction guarantees simultaneous enhancement of light absorption and charge transport, and the Ga_2O_3 layer enables better band alignment that reduces interfacial recombination, increasing the photovoltage. With a photocurrent onset over +1 V against the reversible hydrogen electrode (RHE) and a photocurrent density of ~10 mA cm^{-2} at 0 V versus RHE, this mesoscopic system constitutes by far the best oxide photocathode for catalytic generation of hydrogen from sunlight known today. With X-ray photoelectron and ultraviolet-visible (UV-vis) absorption spectroscopy, we examined the band alignment of Cu_2O with conventionally used aluminium-doped zinc oxide (AZO) and highly optimized Ga_2O_3 in detail, and elucidated the reason for the photovoltage augmentation. Conformal NiMo is coated as the hydrogen evolution catalyst to achieve an all Earth-abundant Cu_2O photocathode with stable operation in a weak alkaline electrolyte, which is more desirable than a neutral electrolyte that entails larger pH gradient losses.

To illustrate the practical impact of the new Cu_2O photocathode, we realized an unassisted solar water splitting with a two-level tandem device using a state-of-the-art $BiVO_4$ photoanode as the top electrode. The remarkable performance of the Cu_2O photocathode enables a near-optimal current match with $BiVO_4$ at a value of 2.45 mA cm^{-2} for overall water splitting, which corresponds to a solar-to-hydrogen

[1]Laboratory of Photomolecular Science, Institute of Chemical Sciences and Engineering, École Polytechnique Fédérale de Lausanne, Lausanne, Switzerland. [2]Laboratory of Photonics and Interfaces, Institute of Chemical Sciences and Engineering, École Polytechnique Fédérale de Lausanne, Lausanne, Switzerland. [3]School of Energy and Chemical Engineering, Ulsan National Institute of Science and Technology, Ulsan, South Korea. [4]Institute of Photoelectronic Thin Film Devices and Technology, College of Electronic Information and Optical Engineering, Nankai University, Tianjin, China. [5]Present address: International Institute for Carbon-Neutral Energy Research (I2CNER), Kyushu University, Fukuoka, Japan. *e-mail: jingshan.luo@nankai.edu.cn; michael.graetzel@epfl.ch

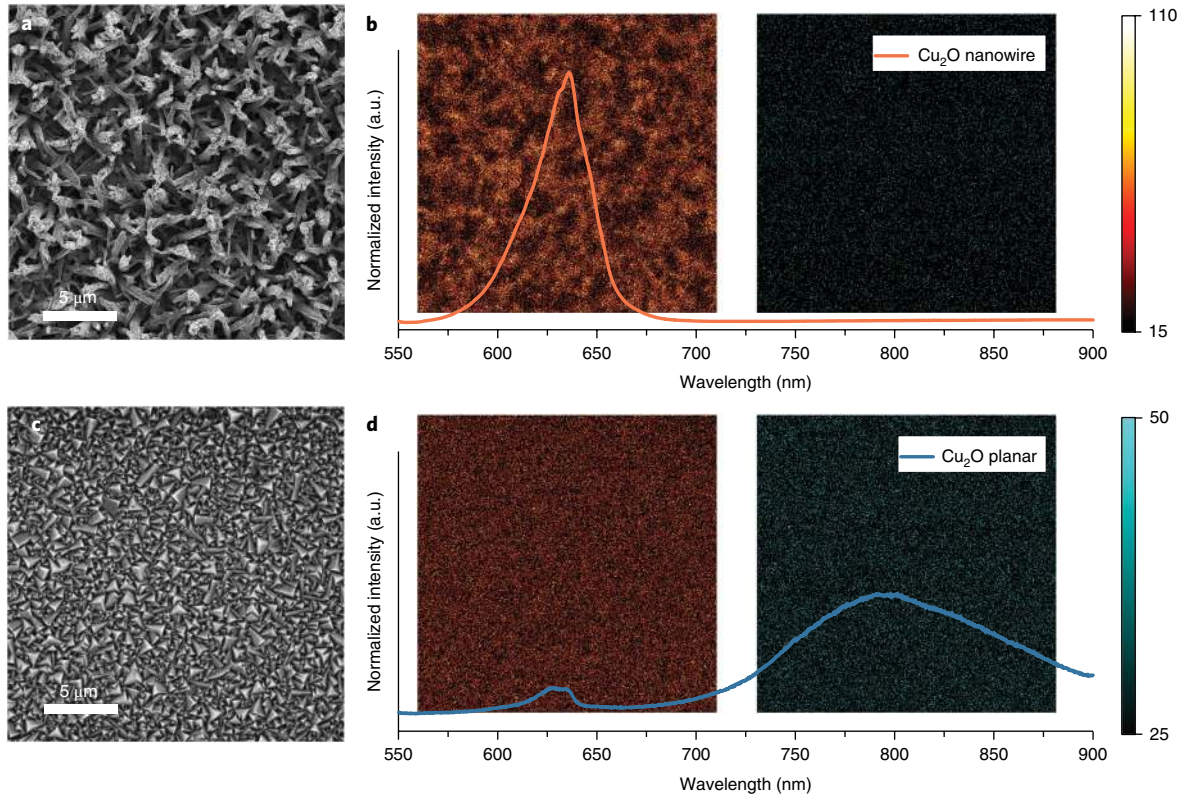

Fig. 1 | SEM imaging and photoluminescence of Cu_2O electrodes. a–d, SEM images (**a** and **c**) and photoluminescence spectra with confocal laser scanning fluorescence mapping (**b** and **d**) of nanowire Cu_2O samples (**a** and **b**) and planar Cu_2O samples (**c** and **d**). The emission between 580 and 680 nm is attributed to the band-edge emission of Cu_2O and assigned an orange colour scale in **b** and **d** (left). The emission between 700 and 800 nm is attributed to emission from the defect states in Cu_2O and assigned a cyan colour scale in **b** and **d** (right). All fluorescence images are 36.90 μm × 36.90 μm. More details on the pseudo-colour assignment can be found in the Methods.

(STH) free-energy conversion efficiency of ~3%. In addition, the stable performance of the Cu_2O photocathode in a weak alkaline electrolyte is a promising indication of the long-term stability of the overall device. Generally, low-cost, unassisted solar water splitting photosystems deliver STH conversion efficiencies below 1% (Supplementary Table 1). The results from this work surpass the performance of all known metal-oxide-based tandem systems that partner with silicon, copper indium gallium selenide or copper zinc tin sulphide.

Results

Material and photoluminescence characterization. The Cu_2O nanowire photoelectrodes were prepared by the electrochemical anodization of copper-coated fluorine-doped SnO_2 (FTO) substrates followed by thermal annealing at 600 °C under an argon atmosphere[8]. The morphology of the electrodes was characterized by scanning electron microscopy (SEM), as illustrated in Supplementary Fig. 1. The nanowires are aligned nearly vertically from the substrate, which is beneficial for enhancing light scattering. On average, their lengths are 3–5 μm and their diameters are 200–400 nm. In the magnified image of a bare Cu_2O nanowire, we observe definite angular morphology with segmented long grains growing along the wire. X-ray diffraction (XRD) patterns reveal the pure cubic Cu_2O phase of the sample with (111) facet as the dominating facet (Supplementary Fig. 2). Except for the unreacted copper on the substrate and the FTO, there are no other chemical constituents. The Cu_2O phase of the sample was verified by Raman spectroscopy (Supplementary Fig. 3)[8,13].

Photoluminescence spectra reflect the quality of Cu_2O electrodes, as the emission is affected by defect states[14,15]. Thus, we carried out steady-state photoluminescence measurements on both the nanowire and the planar Cu_2O photoelectrodes made by electrochemical deposition. Their diverse morphologies can be seen in the top-view SEM images of Fig. 1a,c. The photoluminescence spectra are shown in Fig. 1b,d, respectively. As there is no emission at wavelengths longer than 700 nm, we conclude that the Cu_2O nanowire electrode has few defect states, indicative of its high electronic quality. In contrast, the electrochemically deposited planar Cu_2O electrode shows significant defect-state emission from both oxygen and copper vacancies[14,15]. Furthermore, we obtained photoluminescence maps of both samples using confocal laser scanning microscopy. The emission between 580 and 680 nm is attributed to the band-edge emission of Cu_2O and is assigned an orange colour scale in Fig. 1b,d. The emission between 700 and 800 nm arising from oxygen vacancies is assigned a cyan colour scale. The nanowires are highly emissive in the range 580–680 nm compared with the planar ones, confirming their superior quality for potential use in various optoelectronic applications. In addition, the photoluminescence mapping data reveal the high homogeneity of the surface of our samples.

Band energy-level alignment. Previously, we reported that the nanowire structure can raise the photocurrent density of Cu_2O electrodes[8]. However, the shortcoming of low photovoltage still needs to be addressed. In a Cu_2O heterojunction device, the photovoltage is limited by the quasi-Fermi level difference of the holes in Cu_2O and electrons in the n-type oxide layer under full solar illumination. Hence, choosing an appropriate n-type layer is crucial for achieving high photovoltages. For our Cu_2O nanowire devices, we deposit n-type oxide layers using atomic-layer deposition (ALD) to form coaxial heterojunctions. To investigate the band alignment in detail, we measured UV-vis absorption and X-ray photoelectron

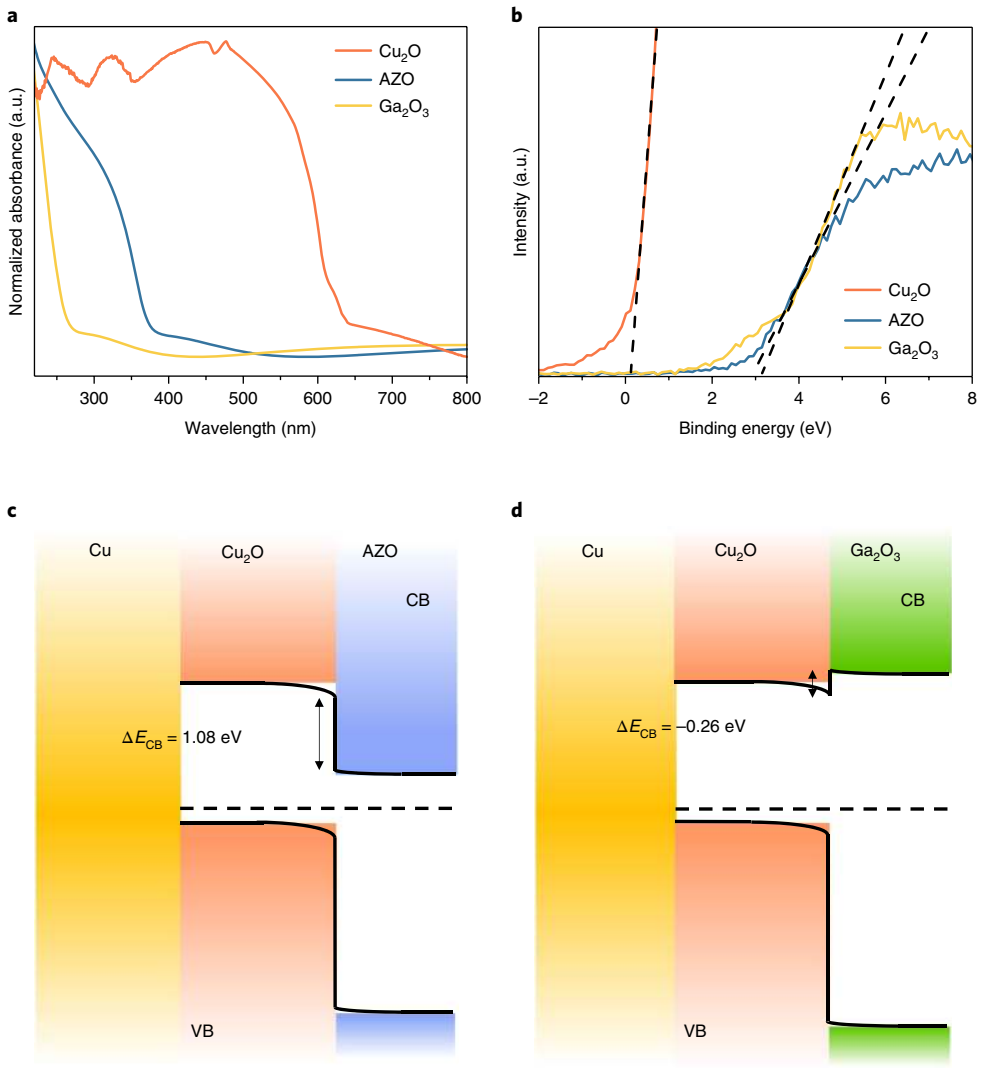

Fig. 2 | Band energy diagrams derived from absorption and XPS measurements. a,**b**, UV-vis absorption spectra (**a**) and valence-band-edge spectra (**b**) of Cu_2O, AZO and Ga_2O_3. **c**,**d**, Equilibrium band-edge diagrams of Cu_2O/AZO (**c**) and Cu_2O/Ga_2O_3 heterojunctions (**d**) with different conduction band (CB) edge discontinuity (ΔE_{CB}) assuming pinning of the band edges of the semiconductors at the interfaces. VB, valence band.

spectroscopy (XPS), and the results are shown in Fig. 2a,b, respectively. Cu_2O, AZO and Ga_2O_3 show optical band gaps of 2, 3.4 and 5 eV, respectively, as derived from Tauc plots assuming a direct allowed transition (Supplementary Fig. 4)[16]. The valence band levels of Cu_2O, AZO and Ga_2O_3 were determined from linear extrapolation of the valence-band-edge spectra measured by XPS. The band offsets were determined by the Kraut method through XPS, using core-level offsets from heterojunction samples and the band gaps of individual samples (Supplementary Fig. 5). Using the optical band gaps and valence band levels, we constructed the band energy-level alignment diagrams of Cu_2O with AZO and Ga_2O_3, as shown in Fig. 2c,d, respectively. A large conduction band offset of 1.08 eV was discovered in the sample with the AZO layer that limits the maximum separation of quasi-Fermi levels in the two oxides under illumination to 0.5 eV in agreement with the 0.5 V positive shift of the onset potential for hydrogen evolution. In contrast, the conduction band offset between the Cu_2O and Ga_2O_3 layer is small, offering a larger energy realm for the splitting of the quasi-Fermi levels between the two oxides under illumination, and hence the build-up of a larger photovoltage. This is despite the spike-type conduction band offset that was formed, which may favour interfacial recombination. Doping the electron-selective layer to raise its donor density can effectively mitigate the recombination, further enhancing the photovoltage.

Cu_2O photoelectrodes with Ga_2O_3 layer and RuO_x catalyst. To fabricate full devices, the core–shell Cu_2O/Ga_2O_3 nanowire arrays were coated with TiO_2 layers using ALD, affording electron conduction and protection against corrosion. To enhance the reduction of water to hydrogen, we deposited RuO_x as the hydrogen evolution catalyst on the surface of the electrode. SEM images (Supplementary Fig. 6) revealed that the $Cu_2O/Ga_2O_3/TiO_2$ nanostructures were conformally covered with the RuO_x layer. Cu_2O nanowire photocathode devices employing AZO and Ga_2O_3 as electron-selective layers were tested in pH 5 electrolyte under chopped illumination (Fig. 3). Compared with the device with the AZO layer, the electrode with Ga_2O_3 shows a 0.5 V anodic shift in onset potential. Remarkably, at +0.5 V versus RHE, where the AZO-based nanowires barely start to deliver a photocurrent, the electrodes using the Cu_2O/Ga_2O_3 junction already produce a photocurrent density of 6.5 mA cm^{-2}.

Moreover, at 0 V versus RHE, the current density reaches almost 10 mA cm^{-2} (Fig. 3a). Comparisons of Cu_2O photocathodes with different n-type layers were made to show the effect of each layer (Supplementary Fig. 7). Bare Cu_2O photocathodes cannot survive

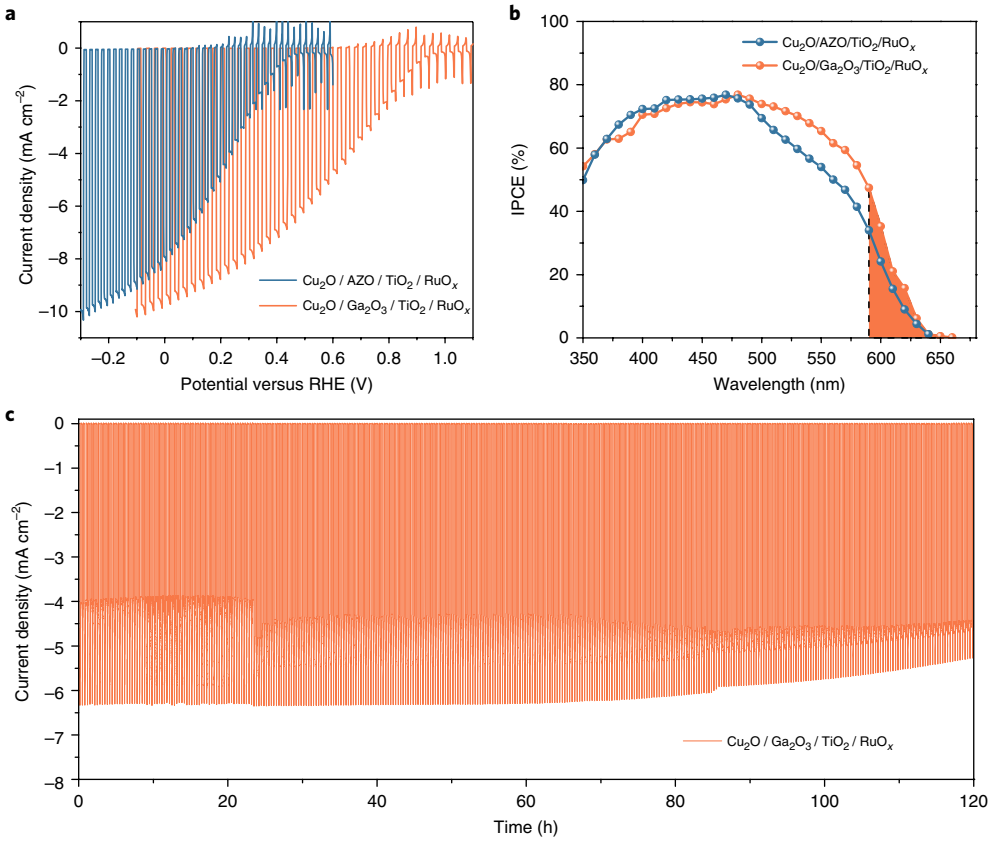

Fig. 3 | PEC performance of Cu_2O nanowire photocathodes. a, *J*–*E* response under simulated one-sun air mass 1.5 G chopped illumination for Cu_2O nanowire photocathodes with AZO/TiO_2/RuO_x and Ga_2O_3/TiO_2/RuO_x. **b**, Corresponding wavelength-dependent IPCE measurements. The shaded area represents the contribution of the excitonic effect to the total quantum yield. **c**, Stability test at a fixed bias of 0.5 V versus RHE with chopped illumination and continuous stirring. The electrolyte was renewed twice during the test. All measurements were performed in a pH 5 electrolyte. Data for the Cu_2O nanowire electrode with AZO as a buffer layer from ref. [8].

one single linear-sweep scan and the current is very low. With a Ga_2O_3 layer on top alone, the large dark current indicates that stability is an issue, as shown in Supplementary Fig. 7b. Here, the dark current accounts for almost one-third of the total current. After coating with a TiO_2 layer, the dark current is suppressed, although the photocurrent is still very low, showing the necessity of the catalyst to utilize the electrons. A PEC test was carried out in 3 different pH electrolytes under standard simulated air mass 1.5 G illumination (Supplementary Fig. 8). Although no apparent current density difference was observed in the region more negative than 0.2 V versus RHE, the onset potential shifted to more positive values when the testing was performed at a higher pH. This is due to the change in the hydrogen bonding energy for different pH values, which has also been reported for other photoelectrodes or hydrogen evolution reaction (HER) catalysts[17,18]. The dark current was negligible across the potential range tested, showing the blocking ability of the heterojunctions. Measurements of the incident photon-to-current conversion efficiency (IPCE) are presented in Fig. 3b. With a broad plateau response across a wide spectral range, the coaxial nanowire photoelectrode clearly outperforms all previously reported systems[7,12]. It is worth mentioning that a considerable improvement in the red light response of the photoelectrode was obtained due to excitonic effects present in our sample. This is highlighted by the shaded area between the electronic band gap (2.1 eV, 590 nm) and optical band gap (1.91 eV, 650 nm) of Cu_2O[19]. The photocurrent in this region accounts for ~6% of the total current.

In addition to the large photocurrent density and high photovoltage, long-term stability is another important challenge for solar water splitting devices. The Cu_2O photocathode with a 100 nm TiO_2 overlayer was tested under continuous stirring and chopped illumination with 10 min intervals for light and dark to simulate intermittent solar irradiation. Impressively, our sample is stable for more than 100 h in a pH 5 electrolyte at a bias potential of +0.5 V versus RHE (Fig. 3c), which is a significant step towards the design of a stand-alone overall PEC water splitting cell in a parallel tandem configuration. Stability under continuous illumination (Supplementary Fig. 9) was also studied with an electrolyte-refreshing strategy similar to a previous report[20]. The performance we demonstrate with a photocurrent density of 10 mA cm^{-2}, a photovoltage exceeding 1 V and stability beyond 100 h sets a new benchmark for Cu_2O towards solar water splitting. To show the wide applicability of the Ga_2O_3 layer on samples with different structures, we also carried out studies on planar Cu_2O samples made by electrochemical deposition. With a similar onset shift obtained for planar Cu_2O samples using a Ga_2O_3 layer (Supplementary Fig. 10), we suggest that the enhancement in photovoltage is solely due to the advantages offered by the Ga_2O_3 layer. With the possibility of making semi-transparent planar Cu_2O photocathodes and achieving higher current density with lower overpotential, improved tandem devices with even higher STH conversion efficiency may be anticipated[21,22].

Distinct from many other metal oxide photoelectrodes for water splitting, the Cu_2O photoelectrode features a buried p–n junction. The origin of the electrical field for charge separation is the p–n junction between Cu_2O and the n-type layer, rather than the semiconductor–electrolyte junction. Thus, the photovoltage of the Cu_2O photoelectrode we measure is the quasi-Fermi level difference

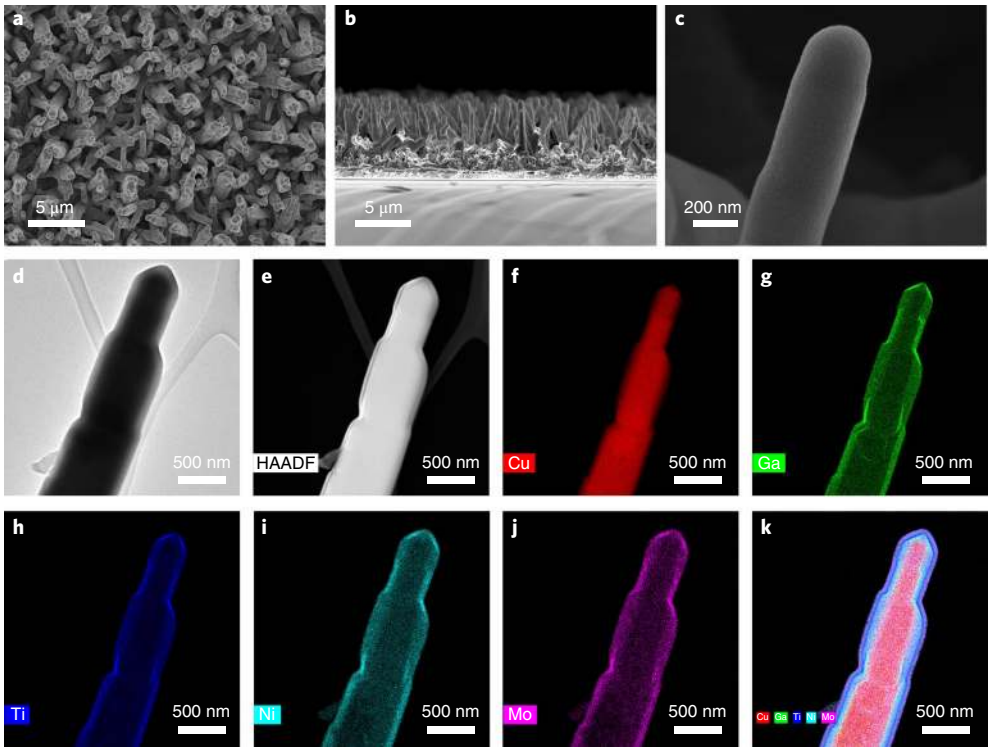

Fig. 4 | Electron microscopy of NiMo-modified Cu_2O photocathodes. a, Top-view SEM image of NiMo-coated Cu_2O nanowire photocathodes. **b**, Cross-sectional image of cleaved Cu_2O photocathodes. **c**, Magnified SEM image focusing on a single nanowire. **d**, High-resolution transmission electron micrograph of a Cu_2O nanowire photoelectrode. **e**, High-angle annular dark-field image of a Cu_2O nanowire photoelectrode. **f**–**j**, Elemental mapping images of Cu, Ga, Ti, Ni and Mo, respectively. **k**, Combined elemental mapping image of Cu Ga, Ti, Ni and Mo.

between the Cu_2O and the n-type layer instead of its flat band potential (Supplementary Fig. 11). We carried out an electrochemical impedance spectroscopy measurement on a bare Cu_2O photoelectrode in pH 9 solution, and the resulting Mott–Schottky plot is shown in Supplementary Fig. 12. Based on the Mott–Schottky equation, the flat band potential of Cu_2O is determined to be +0.70 V versus RHE, which is consistent with the literature[6,8,23]. However, we would not be able to achieve an onset potential more positive than 0.7 V if the onset potential of the Cu_2O photoelectrode is determined by the flat band potential. Moreover, apart from serving as a protection layer, the TiO_2 layer functions as an ohmic contact as its conduction band minimum is well aligned with the hydrogen evolution potential[24]. Thus, here, the conduction band minimum of TiO_2 has no influence on the onset potential of the Cu_2O photocathode. To illustrate the above discussion, band diagrams of Cu_2O/AZO/TiO_2 and Cu_2O/Ga_2O_3/TiO_2 junctions in the dark and under illumination are depicted in Supplementary Fig. 11.

An all Earth-abundant Cu_2O photoelectrode. Although RuO_x is an effective hydrogen evolution catalyst, its scarcity hinders the large-scale deployment of Cu_2O photoelectrodes. In addition, it is not stable in alkaline electrolytes, as demonstrated in Supplementary Fig. 13. The photocurrent dropped by 30% within 8 h in the test using a pH 9 buffer solution. As most of the Earth-abundant electrocatalysts for the oxygen evolution reaction operate in alkaline electrolytes, and tandem devices are imperative for maximizing the utilization of sunlight and driving complete water splitting, it is essential to design our photocathodes to operate in alkaline working environments. Thus, developing a photocathode using an Earth-abundant HER catalyst with stable performance in alkaline electrolytes is of great importance.

A promising substitute for noble metal catalysts, NiMo, showed remarkable activity and stability in alkaline electrolytes[25,26]. Thus, we chose NiMo as the electrocatalyst for our electrode. To estimate the catalytic activity of NiMo, we examined its activity by coating it on nickel foam through electrochemical deposition for 4 min with a current density of −1.5 mA cm^{-2}. After deposition, the rough surface of the nickel foam consisting of visible grains and cavities was uniformly covered with a smooth NiMo catalyst layer (Supplementary Fig. 14). The electrocatalytic performances of both bare nickel foam and NiMo-modified nickel foam were evaluated in three different electrolytes (pH 5, 9 and 12) (Supplementary Fig. 15). In general, at different pH values, the NiMo samples showed similar onset potentials for the HER, whereas different trends in the current density appeared when we scanned to more negative values. The catalyst operating in pH 12 had a steeper slope compared with that obtained for the two other pH values of 5 and 9, leading to overpotentials of 130, 180 and 220 mV at a 10 mA cm^{-2} current density, respectively. This is probably due to different kinetic rates for H_2O dissociation in solutions of different pH levels[27]. The bare nickel foam was also tested as a control experiment. However, the current density contribution from nickel foam at an overpotential of ~200 mV was negligible at different pH levels, clarifying the excellent HER performances of the NiMo catalyst.

We then photoelectrodeposited NiMo onto Cu_2O nanowire photoelectrodes. After deposition, the morphology of the electrode was well preserved (Fig. 4a,b). Taking a closer look, the NiMo catalyst is visible in the form of tiny particles coated homogenously on the surface of the electrode, rivalling the uniformity of ALD and contrasting with previous reports that showed that NiMo aggregated into large particles (Fig. 4c)[28,29]. We further carried out scanning transmission electron microscopy coupled with energy-dispersive X-ray spectroscopy (EDX) elemental mapping measurements on an individual Cu_2O nanowire to closely study the overlayer coating. In Fig. 4d, the bright field image reveals that each Cu_2O nanowire

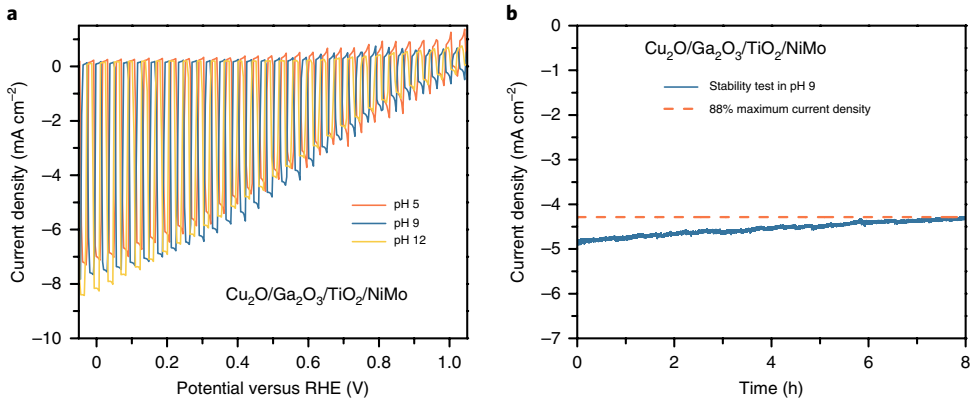

Fig. 5 | PEC measurements on NiMo-modified Cu_2O photocathodes. a, *J*–*E* response under simulated air mass 1.5 G chopped illumination in different pH buffer solutions. **b**, Chronopotentiometry measurement on a NiMo-modified Cu_2O photocathode in pH 9 buffer solution with continuous illumination and stirring.

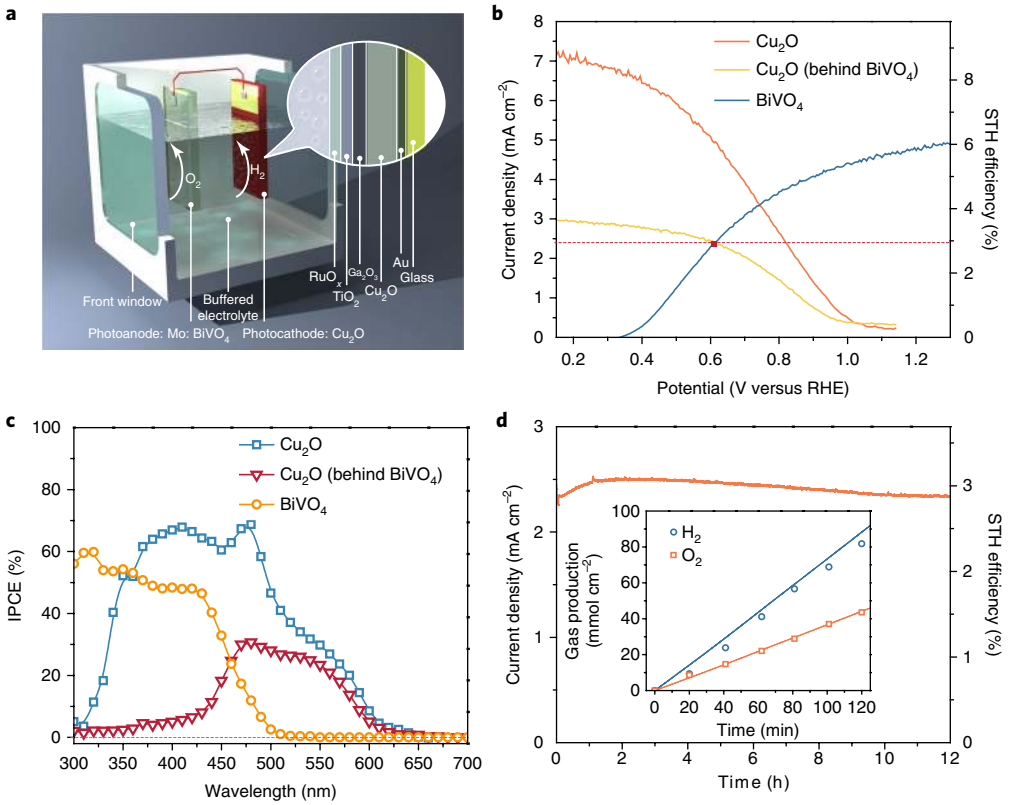

Fig. 6 | Unassisted all-oxide solar water splitting. a, Illustration of the all-oxide tandem solar water splitting device, consisting of Cu_2O as the photocathode and molybdenum-doped $BiVO_4$ (Mo: $BiVO_4$) as the photoanode without bias. **b**, *J*–*E* response under simulated air mass 1.5 G chopped illumination for the Cu_2O photocathode, $BiVO_4$ photoanode and Cu_2O photocathode behind the $BiVO_4$ photoanode in 0.2 M potassium borate (pH 9.0). The crossing point gives ~2.4 mA cm^{-2} and ~3% STH efficiency. **c**, Corresponding wavelength-dependent IPCE spectra. **d**, Unbiased stability test tandem system in 0.2 M potassium borate (pH 9.0). Inset: corresponding gas measurement for both the photocathode and the photoanode.

consists of several large crystal grains connected along one direction. Copper element mapping confirmed this result (Fig. 4e). In the EDX maps (Fig. 4) of other elements, we see that the sequential distribution of each layer forms a radial p–n junction with a well-defined thicknesses for each layer. This enables efficient charge separation and collection, both of which are essential aspects. Moreover, when combined with the homogeneous coating of the NiMo catalyst, effective utilization of charges is ensured, resulting in excellent device performance.

PEC tests were carried out in three electrolytes of different pH values under standard simulated air mass 1.5 G illumination. When NiMo was employed in the nanowire samples, the onset potential was further improved to more than +1.0 V versus RHE for all pH values examined (Fig. 5a). Unlike the RuO_x-modified samples, NiMo-modified samples exhibited similar onset behaviour but showed recognizable differences in the peak current density at 0 V versus RHE. The current density for the NiMo-modified photocathode reaches 8.2 mA cm^{-2} at 0 V versus RHE, which is comparable to that

of the RuO_x-modified sample. The long-term stability of the NiMo-modified Cu_2O nanowire photoelectrodes in an alkaline electrolyte was evaluated under continuous air mass 1.5 G illumination at +0.5 V versus RHE (Fig. 5b). After 8 h, the current density retained ~90% of its maximum value. Considering the excellent stability of NiMo as an electrocatalyst in an alkaline electrolyte, this decrease is probably due to degradation caused by electrolyte penetration into the amorphous TiO_2 layer[25,30]. Detailed degradation mechanisms are currently under investigation. Studies have already shown that treatment of TiO_2 can effectively improve the overall stability[31].

Unassisted overall solar water splitting devices. The ultimate goal in developing high-performance photoelectrodes is to make efficient and stable overall unassisted solar water splitting devices at an affordable cost. This remains a major goal of solar water splitting research. To demonstrate the remarkable performance of the new Cu_2O photocathode, we constructed an unassisted overall solar water splitting tandem device by pairing it with the state-of-the-art $BiVO_4$ photoanode[32,33]. The detailed configuration of the device is shown in Fig. 6a, where the light passes first through the front $BiVO_4$ absorber before reaching the Cu_2O absorber. In this configuration, the wider band gap $BiVO_4$ (2.4 eV) absorbs photons at the high-energy end of the solar spectrum, while lower-energy photons pass through to be absorbed by Cu_2O (2.0 eV band gap). Given that the two photoelectrodes are electronically connected in series, the tandem device current density is limited by the electrode producing the smaller photocurrent, and a balanced generation of photocurrent between the two electrodes is therefore desired. To achieve optimal current matching, we fabricated $BiVO_4$ photoanodes of different transparency by varying the precursor volume. The transmittance of these samples and their associated PEC performances are presented in Supplementary Fig. 16. Although the nanostructured Cu_2O photocathode has a higher plateau current density than the planar one, its comparably low fill factor results in a lower current density at the potential range, which is critical for tandem operation (Supplementary Fig. 17). Thus, we chose the planar Cu_2O samples for the tandem demonstration. The PEC performances of the planar Cu_2O photocathode with and without $BiVO_4$ photoanodes of different transparency as filters are presented in Supplementary Fig. 18. The operating current density of the overall unassisted tandem solar water splitting device can be predicted by overlapping the current density-potential (*J–E)* curves of both electrodes in a front and back configuration and observing the point at which they overlap (Supplementary Fig. 18). The highest current density of ~2.45 mA cm^{-2} was predicted using the $BiVO_4$ photoanode prepared with the 55 µl precursor solution, as illustrated in Supplementary Fig. 19 and Fig. 6b. The IPCE responses of both electrodes show complimentary spectral responses (Fig. 6c). In the wavelength range around 500 nm, where $BiVO_4$ photoanodes almost stop absorbing photons with higher wavelengths, the Cu_2O photocathode still loses a considerable amount of efficiency, which is probably due to scattering and reflection at the electrode surface and the gas–liquid interface. Although the band gaps of both photoelectrodes are not ideal for two-absorber tandem, the absorption mismatch gives reasonable efficiencies.

The stand-alone unassisted solar water device comprising the Cu_2O photocathode and $BiVO_4$ photoanode exhibited a current density as predicted in Fig. 6b. The device showed stable performance with less than 10% loss under continuous illumination for 12 h (Fig. 6d). A peak current density of ~2.5 mA cm^{-2} was achieved after operation for 1 h, which corresponds to an STH conversion efficiency exceeding 3%. To the best of our knowledge, this is by far the highest efficiency reported for unbiased PEC water splitting devices using oxide-only materials (see Supplementary Table 1). A short video of tandem operation is available as Supplementary Video 1. With great advances in the state-of-the-art Cu_2O photocathodes, a huge leap from previous record efficiencies of tandems that combine two absorbers (oxides and silicon, copper indium gallium selenide or copper zinc tin sulphide photoelectrodes) was realized. A gas measurement was also carried out to quantify the H_2 and O_2 gases evolved (Fig. 6d, inset). Owing to the large head space of the PEC cell and the argon purging, the initial Faradaic efficiencies for H_2 and O_2 were not ideal; however, they reached almost 100% afterwards.

Conclusions

In summary, we have demonstrated a benchmark Cu_2O photocathode featuring a current density of 10 mA cm^{-2} at 0 V versus RHE, a photovoltage of 1 V and stability beyond 100 h using a nanostructured Cu_2O absorber, a Ga_2O_3 layer, a TiO_2 protection layer and a RuO_x HER catalyst. Furthermore, an all Earth-abundant Cu_2O photocathode ($Cu/Cu_2O/Ga_2O_3/TiO_2/NiMo$) with stable operation in a weak alkaline electrolyte was achieved. Future work will focus on doping Ga_2O_3 to push up its Fermi level and reduce its resistivity. Moreover, optical spectroscopic measurements are necessary to elucidate the charge-carrier dynamics and excitonic effect in Cu_2O. With this Cu_2O photoelectrode, we constructed an overall unassisted tandem solar water splitting device with a state-of-the-art $BiVO_4$ photoanode, achieving a record STH conversion efficiency of ~3% for all-oxide based devices. Our results provide rational design strategies for making efficient photoelectrodes and push the frontier of PEC water splitting.

Methods

Preparation of Cu_2O nanowire photoelectrodes. FTOs (G2E, TEC-15) were cleaned by sequential ultrasonic treatments in 2% Hellmanex water solution (30 min), acetone (15 min) and deionized water (15 min). Then, 1.5 µm of copper (99.995%) was sputtered on the FTOs using Alliance Concept DP650 with a growth rate of 2.65 nm s^{-1}. Samples were subsequently anodized in 3 M KOH (99.98%, metal basis) solution to form $Cu(OH)_2$ nanowires as a precursor. Using a large-area gold-coated FTO glass as the counter electrode, anodization was performed at a constant current density of 6 mA cm^{-2} at room temperature until a compliance voltage of 2 V was reached. After rinsing with copious amounts of water, the samples were dried in air overnight. To transform $Cu(OH)_2$ into Cu_2O, samples were annealed at 600 °C in a tube furnace under a high-purity argon flow (99.9995%, ALPHAGAZ) for 4 h. Following this, an extra blocking layer of Cu_2O was coated onto the Cu_2O nanowire samples by 30 min electrodeposition in a buffered copper sulphate solution. To prepare the buffered copper sulphate solution, 7.98 g of $CuSO_4$, 21.77 g of K_2HPO_4 and 67.5 g of lactic acid were dissolved in 250 ml of H_2O, and the pH of the electrolyte was adjusted to 12 using a KOH (2 M) solution. The final solution totalled around 1 l. Cu_2O blocking layers were deposited at a constant current density of −0.1 mA cm^{-2} (galvanostatic mode) using a source meter (Keithley 2400) in a two-electrode configuration (a platinum mesh served as the counter electrode). This deposition condition was also used for the preparation of planar Cu_2O samples, with the exception that the deposition time was 100 min.

ALD of overlayers. ALD coating was implemented using a thermal ALD system (Savannah 100, Cambridge NanoTech). The top part of the sample was masked by Kapton tape to protect the electric contact area before the deposition of thin n-type semiconductor layers. To prepare the Cu_2O nanowire samples with an AZO layer, 20 nm of AZO followed by 20 nm of TiO_2 was coated using the previously described configurations[8]. To prepare the Cu_2O nanowire samples with a Ga_2O_3 layer, the exposure mode was employed for better coverage over the nanowires. Gallium oxide was deposited at a substrate temperature of 150 °C using bis(µ-dimethylamino)tetrakis(dimethylamino)digallium (98%; Strem Chemicals) as the gallium precursor and deionized water as the oxidant. The gallium precursor was heated to 130 °C to provide sufficient vapour pressure, and introduced into the chamber under a nitrogen flow of 10 sccm, with a 1 s pulse time, 2 s exposure time and 30 s pumping time. The growth rate for Ga_2O_3 on test silicon wafers with native oxide was determined by ellipsometry (Sopra GES 5E) on test silicon wafers with native oxide, and found to be approximately 1.5 Å per cycle (confirmed by cross-sectional SEM imaging; Supplementary Fig. 20). For all Cu_2O photocathodes with a Ga_2O_3 layer, 135 cycles of Ga_2O_3 were deposited, resulting in a thickness of approximately 20 nm. TiO_2 was deposited at a substrate temperature of 150 °C using Tetrakis(dimethylamino)titanium (99.999%; Sigma) with a precursor temperature of 75 °C. Hydrogen peroxide (50% in water, stabilized; Aldrich) was used as the oxidant. H_2O_2 was stored at 4 °C and the cylinder was freshly refilled before each deposition. Using a nitrogen flow of 5 sccm, TiO_2 was deposited at an approximate growth rate of 0.59 Å per cycle with a 0.1 s pulse time, 2 s exposure time and 30 s pumping time. Deposition cycle numbers were determined by the required thickness and calculated using

the previously mentioned growth rate. Samples for the 100 hour stability test were protected with 100 nm TiO_2 ALD layers and all other samples were protected with 20 nm TiO_2 layers deposited by ALD.

RuO_x hydrogen evolution catalyst deposition. For the RuO_x and NiMo catalysts used in this study, galvanostatic PEC deposition was employed. In the case of the RuO_x deposition, the process used was similar to that previously described[7]. Briefly, the deposition was performed in a 1.3 mM $KRuO_4$ solution at a current density of $-28\,\mu A\,cm^{-2}$ under simulated one-sun illumination. The deposition time was fixed at 6 min. A platinum wire was used as the counter electrode.

NiMo hydrogen evolution catalyst deposition. NiMo was electrodeposited onto nickel foam. Before the deposition, nickel foam was immersed in 32% hydrochloric acid for 3 min to remove the native oxide layer. The solution used for deposition was modified from the one used by ref. [27]. NiMo was deposited from a sulphamate solution with 32.5 g $Ni(SO_3NH_2)_2$, 3 g H_3BO_3 and 0.5 g $NaMoO_4$ in 100 ml solution under constant current for 2 min (current density of $-1.5\,mA\,cm^{-2}$) using a platinum mesh as the counter electrode. Electrodeposition of NiMo on the Cu_2O electrode was carried out under simulated air mass 1.5 G illumination at the same current density as electrodeposition for 180 s. The active area, ranging from 0.25–0.8 cm^2, was determined by applying an opaque epoxy mask before catalyst deposition.

Preparation of $BiVO_4$ films. All of the following chemicals used in this study were of analytical grade and used without further purification. $BiVO_4$ film was prepared by a modified metal–organic decomposition method slightly modified from our previous procedure[32]. Thus, 0.2 M $Bi(NO_3)\bullet 5H_2O$ (99.8%; Kanto Chemical) dissolved in acetic acid (99.7%; Kanto Chemical), 0.03 M $VO(acac)_2$ (98.0%; Sigma–Aldrich) and 0.03 M $MoO_2(acac)_2$ (98.0%; Sigma–Aldrich) in acetyl acetone (>99.0%; Kanto Chemical) were prepared as a precursor solution. Then, a stoichiometric amount of each precursor was mixed to complete a precursor solution. For molybdenum doping, a Bi:(V + Mo) = 1:1 atomic ratio was applied to create 1% molybdenum-doped $BiVO_4$ films. To fabricate the $BiVO_4$ film, ~25–55 µl of solution was dropped on an FTO glass (2 cm × 2.5 cm) and dried for 15 min under an argon atmosphere. The FTO glass (TEC 8; Pilkington) was cleaned using acetone and ethanol with a ratio of 1:5, washed with copious amounts of deionized water and finally stored in acetone before use. The greenish transparent precursor film was calcined at 550 °C for 30 min to form a yellow $BiVO_4$ film. After the annealing process, 2 cm × 2.5 cm $BiVO_4$/FTO was split to obtain photoanodes with a net irradiation area of 0.54 cm^2 connected by silver paste and copper wire and sealed with epoxy resin.

Hydrogen treatment of metal oxide films. Hydrogen treatment was conducted using the borohydride decomposition method reported by ref. [34]. First, 16 mmol of $NaBH_4$ (>98%; Sigma–Aldrich) was placed in a 200 ml alumina crucible and another smaller alumina bottle (15 ml) was put on the $NaBH_4$ powder. In this smaller bottle, as-prepared metal oxide film (2 cm × 2.5 cm) was placed and finally 200 ml alumina crucible was covered with an alumina cover. This reactor was put in furnace, pre-heated to 500 °C, for 30 min. Then, the crucible was immediately taken out from the furnace and naturally cooled down.

$NiFeO_x$ co-catalyst deposition on the $BiVO_4$ film. The $NiFeO_x$ co-catalysts were deposited using photoelectrodeposition under air mass 1.5 G illumination according to the reported procedure with variation based on the NiOOH/FeOOH double-layer oxygen evolution catalyst (OEC)[35]. Some 30 mg of $Fe(SO_4)_2\bullet 7H_2O$ (≥99%; Sigma–Aldrich) and 10 mg of $Ni(SO_4)_2\bullet 6H_2O$ (99%; Sigma–Aldrich) were put in glass bottle and 100 ml of 0.5 M $KHCO_3$ (pH 8.3, 30 min argon gas purged before use) was added, resulting in a transparent and yellow solution. The existence of bicarbonate anions deters premature oxidation of the Fe_2^+ ion to iron hydroxide precipitation, which resembles an orange dust. Photoelectrodeposition was conducted using the as-prepared precursor solution on a photoelectrode. Linear-sweep voltammetry was applied with a bias of −0.3 to 0.5 V versus the reference electrode (Ag/AgCl) ~4–6 times under illumination (air mass 1.5 G, $100\,mW\,cm^{-2}$). Sequential linear-sweep voltammetry gave a reduced current density, suggesting that over-deposition of $NiFeO_x$ could occur at a certain point. After deposition, the photoelectrode was taken out and washed with copious amounts of deionized water. The photoelectrode was stored in a bottle filled with argon gas before use.

Materials characterizations. XRD patterns were acquired using a Bruker D8 DISCOVER diffractometer in the Bragg–Brentano geometry, using copper Kα radiation and a nickel β-filter. Diffraction spectra were recorded between 2θ of 20° and 80° at a scan rate of $1°\,min^{-1}$ with a step width of 0.02°. Raman spectra were carried out on a LabRAM HR Raman spectrometer using a 532 nm laser for excitation. A high-resolution scanning electron microscope (Zeiss Merlin) with an in-lens detector was used for SEM imaging. Transmission electron microscopy was performed on a Tecnai Osiris (FEI) and energy-dispersive X-ray (EDX) elemental mapping was carried out in scanning transmission electron microscopy mode. XPS was carried out using a PHI VersaProbe II scanning XPS microprobe (Physical Instruments AG). Analysis was performed using a monochromatic aluminium Kα X-ray source of 24.8 W power with a beam size of 100 µm. The spherical capacitor analyser was set at a 45° take-off angle with respect to the sample surface. The pass energy was 46.95 eV, yielding a full width at half maximum of 0.91 eV for the silver 3d 5/2 peak. Samples experienced less than 6 min of ambient air exposure during transfer and mounting.

PEC and electrochemical characterization. The PEC performance of samples was evaluated in a three-electrode configuration using Cu_2O photocathodes as the working electrode, a platinum wire as the counter electrode and Ag/AgCl/KCl sat. as the reference electrode. For measurements in solutions of different pH, the pH 5.0 buffer was prepared using a combination of 0.5 M Na_2SO_4 and 0.1 M phosphate solution, while the pH 9.0 buffer was made by adjusting the pH of 0.1 M Na_2CO_3 and 0.1 M $NaHCO_3$ solution, and the pH 12 solution was prepared by tuning the pH of 0.2 M KOH solution. A potentiostat/galvanostat (SP-200; Bio-Logic) was used to acquire the photoresponse under chopped illumination from an LCS-100 solar simulator (class ABB; Newport) with an air mass 1.5 G filter. The PEC cell was fixed at a position determined by measuring the short-circuit current on a calibrated silicon diode with a KG3 filter. Calibration was carried out across the relevant wavelength range of 300–800 nm. All linear-sweep voltammetry scan rates were $10\,mV\,s^{-1}$. The IPCE was measured under light from a 300 W xenon lamp through a monochromator (TLS-300XU; Newport). The photoresponse was compared with that of a calibrated silicon photodiode (FDS100-CAL, Thorlabs) to determine the IPCE at each wavelength. Tests were carried out using chronoamperometry at 0 V versus RHE in a homemade cell with a quartz window (Edmund Optics). A steady current was recorded 5 s later than the wavelength shift with white light-emitting diode light bias to minimize the transient current interference. For the 100 h stability test, the electrolyte was replaced several times. The current density was examined using a chronoamperometry technique at a potential of 0.5 V versus RHE with continuous stirring and light chopping at 10 min intervals for both the light and dark. The electrochemical impedance spectroscopy measurement was carried out for the bare Cu_2O nanowire sample in pH 9 carbonate buffer solution. The space-charge capacitance of the semiconductor varied as a function of the applied potential according to the Mott–Schottky equation shown below. The flat band potential (E_{fb}) and charge-carrier density can be extracted from the x intercept and the slope of the plot using this equation:

$$\left(\frac{A}{C_{bulk}}\right)^2 = \frac{2}{e\varepsilon\varepsilon_0 N_A}\left(E - E_{fb} - \frac{kT}{e}\right)$$

where e is the electron charge, $\varepsilon = 7.5$ is used as the relative permittivity of Cu_2O[36], ε_0 is the permittivity of the vacuum, T is the thermodynamic temperature and E is the applied potential. As shown in Supplementary Fig. 11, the flat band potential is about +0.70 V versus RHE and the carrier concentration is around $1.40 \times 1{,}018\,cm^{-3}$, which agrees with previous results[23,37]. Potential values were transformed to the reversible hydrogen electrode scale using the equation: $E_{RHE} = E_{Ag/AgCl(KCl\ sat.)} + 0.197\,V + 0.059\,V * pH$ (where 'sat.' is saturated).

PEC measurements of the photoanodes and tandem system were performed with standard three-electrode configurations; that is, the photoanode as the working electrode, the platinum mesh as the counter electrode and Ag/AgCl (3 M NaCl) as the reference electrode. The scan rate for the current-voltage (J–V) curve was $20\,mV\,s^{-1}$. For the water oxidation experiments, 0.2 M potassium borate electrolyte (made using deionized water, 1.0 M KOH (>99%; Samjun) and H_3BO_3 (≥99%; Sigma–Aldrich) (pH ~9.0) was used as the main electrolyte. An electrolyte purged with argon gas (30 min) was used to remove dissolved oxygen. To measure the degree of charge separation, 1.0 M Na_2SO_3 (>98%; Sigma–Aldrich) was added to the main electrolyte. Potentials were recorded with correction by the Nernst relation $E_{RHE} = E_{Ag/AgCl(KCl\ sat.)} + 0.197\,V + 0.059\,V * pH$, in which $E_{Ag/AgCl}$ is the applied bias potential and 0.209 is a conversion factor from the Ag/AgCl electrode to the RHE scale. All electrochemical data were recorded using a potentiostat (IviumStat, Ivium Technologies). A 300 W xenon lamp was used to produce simulated one-sun light irradiation conditions (air mass 1.5 G, $100\,mW\,cm^{-2}$) using a solar simulator (Oriel 91160) with an air mass 1.5 G filter calibrated with a reference cell certified by the National Renewable Energy Laboratory.

PEC H_2 and O_2 evolution measurements. Using argon as a carrier gas, the amounts of H_2 and O_2 gases evolved from the PEC cell were analysed using a gas chromatograph (HP 5890, molecular sieve 5 l column) equipped with a thermal conductivity detector. The light source and electrolyte were the same as those used for the above PEC measurements, and the gas products were sampled every 20 min.

Optical measurements. The UV-vis absorption spectra of the AZO and Ga_2O_3 samples on quartz substrates were characterized using a UV-vis-NIR Spectrophotometer (Cary) in transmission mode, and the absorption spectra of Cu_2O were derived from the Kubelka–Munk theory using diffuse reflectance spectra measured with an integrating sphere. The UV-vis absorbance of the $BiVO_4$ film was measured using a UV-vis spectrometer (UV-2401PC, Shimadzu). As a reference, BaSO4 powder attached to FTO was used. The optical band gaps of Cu_2O, AZO and Ga_2O_3 were determined from liner extrapolation of Tauc plots, assuming direct allowed transition ($n = 1/2$). Steady-state photoluminescence

spectra were acquired with a LabRAM HR Raman spectrometer with a 532 nm laser for excitation. Confocal laser scanning fluorescence images were captured at 25 °C using Leica Application Suite X software on a confocal laser scanning microscope (Leica TCS SP8). A harmonic compound plan apochromatic oil objective (63×/1.40) was used. A pulsed white light laser (set at 514 nm) was used for excitation. Identical excitation power and gain settings (values set to obtain the best dynamic range of the photomultiplier tube detectors) were used to capture both images (and both channels in each image). Single-plane 512 × 512 images were obtained from a unidirectional scan (400 Hz speed) with a line accumulation of 12. The pinhole size was 1 Airy unit. Acquisition was done at a resolution of 72 nm in *xy* and an image bit depth of 8. Both channels were pseudo-coloured. Then, linear brightness and contrast adjustments were performed equally to identical channels in both images. The scale bars for the pseudo-colour assignment after these adjustments are shown with the images.

Data availability. The data that support the plots within this paper and other finding of this study are available from the corresponding author upon reasonable request.

Received: 25 May 2017; Accepted: 17 April 2018;
Published online: 21 May 2018

References

1. Luo, J. Water photolysis at 12.3% efficiency via perovskite photovoltaics and Earth-abundant catalysts. *Science* **345**, 1593–1597 (2015).
2. Walter, M. G. et al. Solar water splitting cells. *Chem. Rev.* **110**, 6446–6473 (2010).
3. Ager, J. W., Shaner, M. R., Walczak, K. A., Sharp, I. D. & Ardo, S. Experimental demonstrations of spontaneous, solar-driven photoelectrochemical water splitting. *Energy Environ. Sci.* **8**, 2811–2824 (2015).
4. Osterloh, F. E. Inorganic nanostructures for photoelectrochemical and photocatalytic water splitting. *Chem. Soc. Rev.* **42**, 2294–2320 (2013).
5. Sivula, K. & van de krol, R. Semiconducting materials for photoelectrochemical energy conversion. *Nat. Rev. Mater.* **1**, 15010 (2016).
6. Paracchino, A., Laporte, V., Sivula, K., Grätzel, M. & Thimsen, E. Highly active oxide photocathode for photoelectrochemical water reduction. *Nat. Mater.* **10**, 456–461 (2011).
7. Tilley, S. D., Schreier, M., Azevedo, J., Stefik, M. & Grätzel, M. Ruthenium oxide hydrogen evolution catalysis on composite cuprous oxide water splitting photocathodes. *Adv. Funct. Mater.* **24**, 303–311 (2014).
8. Luo, J. et al. Cu_2O nanowire photocathodes for efficient and durable solar water splitting. *Nano Lett.* **16**, 1848–1857 (2016).
9. Minami, T., Nishi, Y. & Miyata, T. Effect of the thin Ga_2O_3 layer in n^+-ZnO/n-Ga_2O_3/p-Cu_2O heterojunction solar cells. *Thin Solid Films* **549**, 65–69 (2013).
10. Minami, T., Nishi, Y. & Miyata, T. High-efficiency Cu_2O-based heterojunction solar cells fabricated using a Ga_2O_3 thin film as n-type layer. *Appl. Phys. Express* **6**, 44101 (2013).
11. Lee, Y. S. et al. Atomic layer deposited gallium oxide buffer layer enables 1.2 v open-circuit voltage in cuprous oxide solar cells. *Adv. Mater.* **26**, 4704–4710 (2014).
12. Li, C. et al. Positive onset potential and stability of Cu_2O-based photocathodes in water splitting by atomic layer deposition of a Ga_2O_3 buffer layer. *Energy Environ. Sci.* **8**, 1493–1500 (2015).
13. Jiang, T. et al. Copper borate as a photocathode in p-type dye-sensitized solar cells. *RSC Adv.* **6**, 1549–1553 (2016).
14. Ito, T. & Masumi, T. Detailed examination of relaxation processes of excitons in photoluminescence spectra of Cu_2O. *J. Phys. Soc. Jpn.* **66**, 2185–2193 (1997).
15. Li, J. et al. Engineering of optically defect free Cu_2O enabling exciton luminescence at room temperature. *Opt. Mater. Express* **3**, 2072 (2013).
16. Viezbicke, B. D., Patel, S., Davis, B. E. & Birnie, D. P. Evaluation of the Tauc method for optical absorption edge determination: ZnO thin films as a model system. *Phys. Status Solidi.* **252**, 1700–1710 (2015).
17. Brandt, R. E. et al. Band offsets of n-type electron-selective contacts on cuprous oxide (Cu_2O) for photovoltaics. *Appl. Phys. Lett.* **105**, 263901 (2014).
18. Kraut, E. A., Grant, R. W., Waldrop, J. R. & Kowalczyk, S. P. Precise determination of the valence-band edge in X-ray photoemission spectra: application to measurement of semiconductor interface potentials. *Phys. Rev. Lett.* **44**, 1620–1623 (1980).
19. Omelchenko, S. T., Tolstova, Y., Atwater, H. A. & Lewis, N. S. Excitonic effects in emerging photovoltaic materials: a case study in Cu_2O. *ACS Energy Lett.* **2**, 431–437 (2017).
20. Kuang, Y. et al. Ultrastable low-bias water splitting photoanodes via photocorrosion inhibition and in situ catalyst regeneration. *Nat. Energy* **2**, 16191 (2016).
21. Dias, P. et al. Transparent cuprous oxide photocathode enabling a stacked tandem cell for unbiased water splitting. *Adv. Energy Mater.* **5**, 1–9 (2015).
22. Son, M.-K. et al. A copper nickel mixed oxide hole selective layer for Au-free transparent cuprous oxide photocathodes. *Energy Environ. Sci.* **10**, 912–918 (2017).
23. Xu, Q. et al. Electrodeposition of Cu_2O nanostructure on 3D Cu micro-cone arrays as photocathode for photoelectrochemical water reduction. *J. Electrochem. Soc.* **163**, H976–H981 (2016).
24. Seger, B. et al. Using TiO_2 as a conductive protective layer for photocathodic H_2 evolution. *J. Am. Chem. Soc.* **135**, 1057–1064 (2013).
25. McKone, J. R., Sadtler, B. F., Werlang, C. A., Lewis, N. S. & Gray, H. B. Ni–Mo nanopowders for efficient electrochemical hydrogen evolution. *ACS Catal.* **3**, 166–169 (2013).
26. Wang, Y. et al. A 3D nanoporous Ni–Mo electrocatalyst with negligible overpotential for alkaline hydrogen evolution. *ChemElectroChem* **1**, 1138–1144 (2014).
27. Strmcnik, D., Lopes, P. P., Genorio, B., Stamenkovic, V. R. & Markovic, N. M. Design principles for hydrogen evolution reaction catalyst materials. *Nano Energy* **29**, 29–36 (2016).
28. McKone, J. R. et al. Evaluation of Pt, Ni, and Ni–Mo electrocatalysts for hydrogen evolution on crystalline Si electrodes. *Energy Environ. Sci.* **4**, 3573–3583 (2011).
29. Morales-Guio, C. G. et al. Photoelectrochemical hydrogen production in alkaline solutions using Cu_2O coated with earth-abundant hydrogen evolution catalysts. *Angew. Chem. Int. Ed.* **54**, 664–667 (2015).
30. Krstajić, N. V. et al. Electrodeposition of Ni–Mo alloy coatings and their characterization as cathodes for hydrogen evolution in sodium hydroxide solution. *Int. J. Hydrog. Energy* **33**, 3676–3687 (2008).
31. Azevedo, J. et al. On the stability enhancement of cuprous oxide water splitting photocathodes by low temperature steam annealing. *Energy Environ. Sci.* **7**, 4044–4052 (2014).
32. Kim, J. H. et al. Wireless solar water splitting device with robust cobalt-catalyzed, dual-doped $BiVO_4$ photoanode and perovskite solar cell in tandem: a dual absorber artificial leaf. *ACS Nano* **9**, 11820–11829 (2015).
33. Kim, J. H. et al. Hetero-type dual photoanodes for unbiased solar water splitting with extended light harvesting. *Nat. Commun.* **7**, 13380 (2016).
34. Hao, Y., Deng, J., Zhou, L., Sun, X. & Zhong, J. Depth-reduction induced low onset potential of hematite photoanodes for solar water oxidation. *RSC Adv.* **5**, 31086–31090 (2015).
35. Li, F. et al. An iron-based thin film as a highly efficient catalyst for electrochemical water oxidation in a carbonate electrolyte. *Chem. Commun.* **52**, 5753–5756 (2016).
36. Hodby, J. W., Jenkins, T. E., Schwab, C., Tamura, H. & Trivich, D. Cyclotron resonance of electrons and of holes in cuprous oxide, Cu_2O. *J. Phys. C. Solid State Phys.* **9**, 1429–1439 (1976).
37. Li, C., Li, Y. & Delaunay, J. J. A novel method to synthesize highly photoactive Cu_2O microcrystalline films for use in photoelectrochemical cells. *ACS Appl. Mater. Interfaces* **6**, 480–486 (2014).

Acknowledgements

The authors thank P. Mettraux for XPS measurements, and L. Yao, X. Yu and K. Sivula for Raman and steady-state photoluminescence measurements. This work was supported by the following projects: National Research Programme 'Energy Turnaround' (NRP 70) of the Swiss National Science Foundation; PECHouse3, funded by the Swiss Federal Office of Energy under contract SI/500090-03; PECDEMO, co-funded by Europe's Fuel Cell and Hydrogen Joint Undertaking (621252); the Marie Skłodowska-Curie Fellowship (awarded to J.L.) from the European Union's Seventh Framework Programme for research, technological development and demonstration under grant agreement 291771; the Thousand Talents Plan for young professionals (awarded to J.L.); and the European Union's Horizon 2020 programme, through an FET-Open research and innovation action under grant agreement 687008.

Author contributions

L.P., J.L. and M.T.M. conceived and designed the experiment. L.P. and J.H.K carried out device fabrication, characterization and testing. M.T.M. conducted the Ga_2O_3 ALD deposition. M.-K.S. conducted the IPCE measurements. A.U. conducted the confocal laser scanning microscopy measurements. J.L. conducted the XRD, transmission electron microscopy and UV-vis characterizations. L.P. and J.L. wrote the first draft. J.L. and M.G. directed the work. J.S.L. and A.H. provided constructive advice. All authors discussed the results and contributed to the manuscript.

Competing interests

The authors declare no competing interests.

Additional information

Supplementary information is available for this paper at https://doi.org/10.1038/s41929-018-0077-6.

Reprints and permissions information is available at www.nature.com/reprints.

Correspondence and requests for materials should be addressed to J.L. or M.G.

Publisher's note: Springer Nature remains neutral with regard to jurisdictional claims in published maps and institutional affiliations.